

# MDAMF: Reconstruction of Cardiac Cine MRI under Free-breathing using Motion-guided Deformable Alignment and Multi-resolution Fusion\*

Xiaoxiang Han<sup>a</sup>, Yiman Liu<sup>b,c</sup>, Yuanjie Lin<sup>a</sup>, Keyan Chen<sup>a</sup>, Weikun Zhang<sup>a</sup>, Qiaohong Liu<sup>d,\*</sup>

<sup>a</sup>*School of Health Sciences and Engineering, University of Shanghai for Science and Technology, Shanghai, 200093, China*

<sup>b</sup>*Department of Pediatric Cardiology, Shanghai Children's Medical Center, School of Medicine, Shanghai Jiao Tong University, Shanghai, 200127, China*

<sup>c</sup>*Shanghai Key Laboratory of Multidimensional Information Processing, School of Communication & Electronic Engineering, East China Normal University, Shanghai, 200241, China*

<sup>d</sup>*School of Medical Instruments, Shanghai University of Medicine and Health Sciences, Shanghai, 201318, China*

## Abstract

Cardiac cine magnetic resonance imaging not only requires higher imaging speed but also needs to address motion artifacts. Especially in the case of free-breathing, more motion artifacts are inevitably introduced. This poses higher demands on the reconstruction performance of the model and its ability to capture temporal information. Previous methods have not effectively utilized the temporal dimension information to compensate for motion artifacts. In order to fully leverage the spatiotemporal information and reduce the impact of motion artifacts, this paper proposes a motion-guided deformable alignment method with second-order bidirectional propagation. Furthermore, aligning adjacent frames may lead to low accuracy or misalignment issues, which are detrimental to subsequent fusion reconstruction. Previous methods have not sufficiently integrated and corrected the aligned feature information. This paper proposes a multi-resolution fusion method to further correct alignment errors or artifacts. Compared to other advanced methods, the proposed approach achieves better image reconstruction quality in terms of peak signal-to-noise ratio (PSNR), structural similarity index (SSIM), and visual effects. The source code will be made available on <https://github.com/GtLinyer/MDAMF>.

**Keywords:** Cardiac Cine MRI, MRI Reconstruction, Motion-guided, Free-breathing, Multi-resolution

## 1. Introduction

MRI is a widely used diagnostic tool in clinical practice, offering advantages such as non-invasiveness, absence of ionizing radiation, and multiple parameters. However, due to physiological and hardware limitations,

MRI examinations tend to be slower compared to other imaging modalities. Cine MRI, as an integral part of MRI technology, allows for the continuous assessment of organ anatomy and the dynamic effects of physiological and pathological mechanisms in both the temporal and spatial domains. Unlike conventional two-dimensional static MRI images, cine MRI contains valuable information in the temporal dimension. Consequently, cine MRI finds extensive applications in cardiac imaging, flow imaging, and cardiovascular disease diagnosis. Particularly in the context of cardiac cine MRI reconstruction, there is a higher demand for imaging speed while also dealing with motion artifacts. Therefore, the improvement of recon-

\*This research was partially supported by the National Natural Science Foundation of China (Project No. 61801288)

\*Corresponding Author.

Email addresses: [glinyer@163.com](mailto:glinyer@163.com) (Xiaoxiang Han), [LiuyimanSCMC@163.com](mailto:LiuyimanSCMC@163.com) (Yiman Liu), [linyuanjie0312@163.com](mailto:linyuanjie0312@163.com) (Yuanjie Lin), [albertchendev@163.com](mailto:albertchendev@163.com) (Keyan Chen), [zwk7799@163.com](mailto:zwk7799@163.com) (Weikun Zhang), [hql1qh@163.com](mailto:hql1qh@163.com) (Qiaohong Liu)

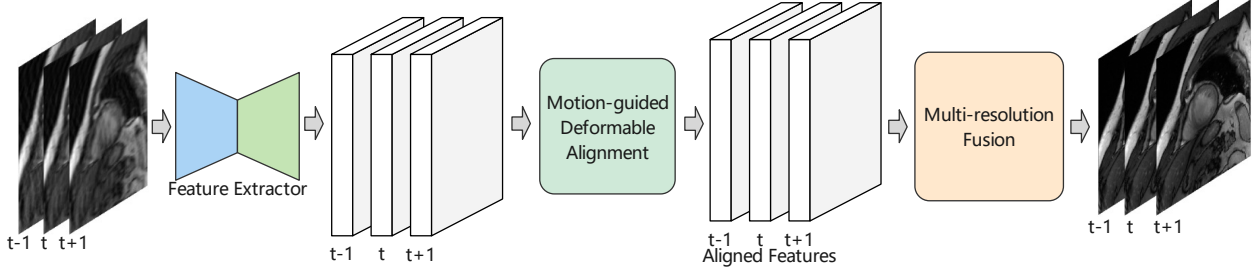


Figure 1: Overall architecture of the proposed method.

struction algorithms holds significant importance for the widespread application of cardiac cine MRI imaging technology.

Collecting fewer k-space data during magnetic resonance imaging is the mainstream approach for MRI acceleration. However, due to violating the Nyquist theorem, directly performing Fourier inverse transformation on zero-filled and undersampled k-space data will result in images with aliasing artifacts. In the past, methods for recovering fully sampled MRI signals included partial Fourier transform [1], parallel imaging (PI) [2], compressed sensing (CS) [3], low-rank matrix completion [4], and manifold learning [5]. However, with the development of deep learning, reconstruction methods based on deep learning have surpassed the aforementioned methods. In 2016, Wang et al. [6] were the first to introduce deep learning into MRI reconstruction tasks. They used convolutional neural networks to establish a mapping relationship between a large number of undersampled images and fully sampled images, and then, during prediction, only inputted the undersampled images to obtain high-quality reconstructed images. Since then, numerous 2D MRI reconstruction algorithms based on deep learning have emerged [7, 8, 9, 10, 11].

Although significant progress has been made in static magnetic resonance imaging (MRI) reconstruction, only a few studies have applied deep learning to cine MRI reconstruction or cardiac cine MRI reconstruction. In earlier work, Odille et al. [12] used a compressed sensing-based approach for the reconstruction of dynamic cardiac MRI under free breathing. Similarly, Chandarana et al. [13] employed a similar technique for the reconstruction of dynamic liver under free breathing. Other related works include [14, 15]. However, due to the lim-

ited modeling capability of these methods, which did not utilize deep learning techniques, the reconstruction results were often unsatisfactory. With the development of deep learning, some studies have emerged that apply this technology to cine MRI reconstruction. Chlempner et al. [16] introduced a data sharing (DS) layer in a 2D reconstruction model to regularize the temporal correlation between different frames of cine MRI. Qin et al. [17] proposed CRNN, which utilizes convolutional recurrent neural networks to handle dynamic signals and employs bidirectional recurrent hidden connections across time sequences to learn spatiotemporal correlations. Sarasaen et al. [18] fine-tuned the network using static high-resolution MRI as prior knowledge. Additionally, there are some unsupervised methods [19, 20, 21]. Since motion information is an important prior in cine MRI, some studies [22, 23] have improved cine MRI reconstruction by leveraging motion information. Although these works focus on dynamic MRI reconstruction and some also consider motion artifacts, they are not specifically designed for free-breathing scenarios. Eldeniz et al. [24] explored deep learning-based reconstruction of dynamic liver MRI under free breathing. Kunz et al. [25] developed a model specifically for cine cardiac MRI reconstruction under free breathing using deep learning. Similar works include [26, 27]. However, these methods do not fully exploit the temporal information to compensate for motion artifacts and do not adequately fuse and correct aligned feature information. To address these issues, this paper proposes a method for reconstructing cine cardiac MRI under free breathing based on **Motion-guided Deformable Alignment and Multiresolution Fusion (MDAMF)**.

The main contributions of this paper are as follows.

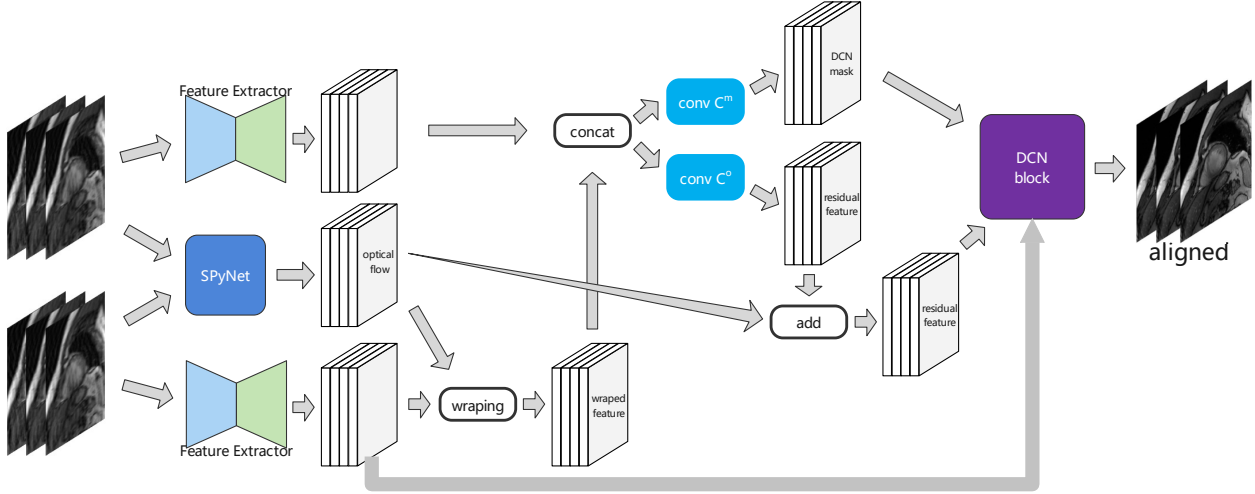


Figure 2: Motion-guided deformable alignment module.

1. We present a novel motion-guided deformable alignment method with second-order bidirectional propagation that effectively utilizes spatiotemporal information in cine MRI and mitigates the impact of artifacts.
2. We propose a multi-resolution fusion method, which is an architecture that combines Transformer and CNN, to further correct alignment errors or artifacts that may arise.
3. We evaluated the proposed method on two public datasets and demonstrated its superiority over existing methods. We also conducted an ablation study to confirm the effectiveness of our approach. Our experimental results show that the proposed method outperforms other state-of-the-art methods in terms of PSNR, SSIM, and visual quality.

## 2. Proposed Method

### 2.1. Problem statement

Dynamical magnetic resonance reconstruction is formally an optimization problem, where a set of undersampled k-space data  $\{y_f\}_{f \in [F]}$  from several frames of a given slice is used to predict  $\{\theta\}$  from  $\{y_f\}$  through a deep neural network.

$$\theta^* = \operatorname{argmin}_{\theta} \sum_{f=1}^F \frac{1}{2} \|F_u(\theta) - f_y\|_2^2 + \lambda R(\theta) \quad (1)$$

The first fidelity term  $\|F_u(\theta) - f_y\|$  is used to ensure data consistency by constraining the reconstructed image  $\theta$  to be close to the input value  $y_f$ . The operator  $F_u(\cdot)$  transforms the image domain  $\theta$  into the frequency domain and then performs undersampling. The second term  $F_u(\cdot)$  is a regularization function that depends on prior knowledge of the input  $y_f$ .  $\lambda$  is a weighting factor. In the proposed method, motion information is an important prior knowledge.

### 2.2. Motion-guided deformable alignment

Deformable convolution has been applied to video super-resolution reconstruction [28], in which 2D displacements are added to the lattice sampling positions of standard convolution rules, allowing the sampling grid to deform freely. Since the displacement here needs to be learned from the previous layer features through another convolution layer, the deformation is local, dense, and adaptive to the input features [29]. However, DCN is difficult to train and the training process is unstable, and it may even cause offset overflow [30]. Therefore, we propose to use motion information to guide the learning of offsets in DCN. Usually, motion information can be

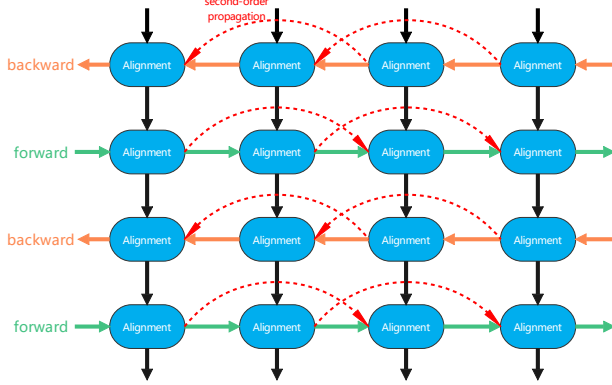


Figure 3: Second-order grid propagation.

obtained through optical flow estimation. However, traditional optical flow calculation requires a large amount of computation, so we use pre-trained SPyNet for optical flow estimation. The structure of the alignment module is shown in Fig. 2.

To make use of alignment features from further in the past or future, we introduce second-order grid propagation, where the current state not only receives hidden states from adjacent grid points, but also from points further away, as shown in Fig. 3. This approach improves the flow of information in the network by introducing second-order Markovian properties, allowing for additional spatial positional features to be obtained during frame alignment [31].

The expression of each grid point in the forward propagation process is as follows:

$$s_{i \rightarrow i-1}, s_{i \rightarrow i-2} = \mathcal{M}(x_i, x_{i-1}), \mathcal{M}(x_i, x_{i-2}) \quad (2)$$

$$\hat{f}_i^j = \mathcal{A} \langle g_i, f_{i-1}^j, f_{i-2}^j, s_{i \rightarrow i-1}, s_{i \rightarrow i-2} \rangle \quad (3)$$

In the equations above,  $x_i$  represents the input image at time step  $i$ .  $g_i$  represents the feature map obtained by extracting features from the input image at time step  $i$ .  $f_i^j$  represents the aligned and corrected feature map at time step  $i$  for the  $j$ th branch. When  $j=0$ ,  $f_i^0$  is equal to  $g_i$ .  $\hat{f}_i^j$  represents the feature map after motion-guided deformable alignment, which contains all the alignment information from the previous time steps  $i-1$  and  $i-2$ .  $s_{i \rightarrow i-1}$  and  $s_{i \rightarrow i-2}$  represent the optical flow between frame  $i$  and frames  $i-1$  and  $i-2$ , respectively.  $\mathcal{M}(\cdot)$

denotes motion estimation, which is performed using pre-trained SPyNet for optical flow estimation.

Next, the aligned feature maps from the backward branch and the aligned feature maps from the forward branch are concatenated, and then sent to the feature correction module for improvement, with the specific expression as follows:

$$f_i^j = \hat{f}_i^j + \mathcal{R}es \langle \mathcal{C}at(f_i^{j-1}, \hat{f}_i^j) \rangle \quad (4)$$

where  $\mathcal{C}at(\cdot, \cdot)$  represents concatenation and  $\mathcal{R}es(\cdot)$  represents a stacked residual block.

The alignment operation under the second-order propagation is as follows, where  $\mathcal{W}(\cdot, \cdot)$  represents pre-alignment:

$$\tilde{f}_{i-1} = \mathcal{W}(f_{i-1}, s_{i \rightarrow i-1}) \quad (5)$$

$$\tilde{f}_{i-2} = \mathcal{W}(f_{i-2}, s_{i \rightarrow i-2}) \quad (6)$$

Then, the results of alignment using optical flow  $\tilde{f}_{i-1}$ ,  $\tilde{f}_{i-2}$  and optical flow  $s_{i \rightarrow i-1}$ ,  $s_{i \rightarrow i-2}$  are used to guide the learning of offsets and modulated scalars in DCN, by learning 2 offsets and modulation masks by merging 3 frames.

$$o_{i \rightarrow i-p} = s_{i \rightarrow i-p} + \mathcal{C}^o \langle \mathcal{C}at(g_i, \tilde{f}_{i-1}, \tilde{f}_{i-2}) \rangle \quad (7)$$

$$m_{i \rightarrow i-p} = \text{Sigmoid} \langle \mathcal{C}^m \langle \mathcal{C}at(g_i, \tilde{f}_{i-1}, \tilde{f}_{i-2}) \rangle \rangle \quad (8)$$

where  $\mathcal{C}^o(\cdot)$  and  $\mathcal{C}^m(\cdot)$  are stacks of convolutional neural network layers, and  $p=1,2$ .

Next, the learned offsets and modulation masks are merged to generate the final offsets ( $o_i$ ) and modulation masks ( $m_i$ ) used for DCN.

$$o_i = \mathcal{C}at(o_{i \rightarrow i-1}, o_{i \rightarrow i-2}) \quad (9)$$

$$m_i = \mathcal{C}at(m_{i \rightarrow i-1}, m_{i \rightarrow i-2}) \quad (10)$$

$$\bar{f}_i = \mathcal{DCN}(\mathcal{C}at(f_{i-1}, f_{i-2}); o_i, m_i) \quad (11)$$

### 2.3. Multi-resolution fusion

Cine magnetic resonance imaging (MRI) requires careful consideration of both inter-frame and intra-frame correlations. Support frames may contain artifacts such as ghosting and blurring. Moreover, misalignment between adjacent frames during fusion may lead to blurred images and affect subsequent reconstruction.

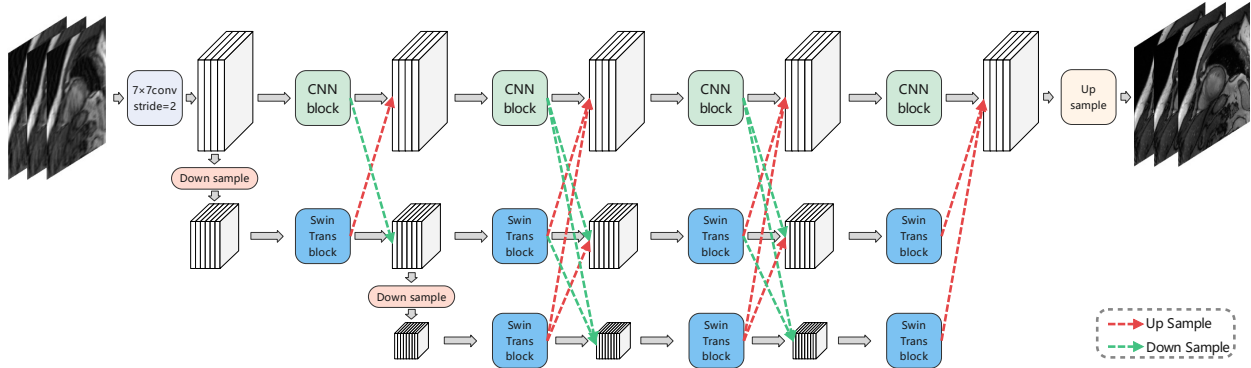


Figure 4: Multi-resolution fusion module.

Table 1: Quantitative comparison results on the ACDC dataset.

Method	4×			8×		
	PSNR (dB) $\uparrow$	SSIM (%) $\uparrow$	NMSE $\downarrow$	PSNR (dB) $\uparrow$	SSIM (%) $\uparrow$	NMSE $\downarrow$
undersample	28.39	67.88	0.0868	25.70	56.31	0.1532
ESPIRiT	$28.96 \pm 1.26$	$74.08 \pm 4.82$	$0.0692 \pm 0.0085$	$25.92 \pm 1.33$	$60.49 \pm 4.97$	$0.1321 \pm 0.0060$
kt FOCUSS	$29.14 \pm 1.22$	$74.26 \pm 4.25$	$0.0651 \pm 0.0075$	$26.02 \pm 1.27$	$61.84 \pm 5.18$	$0.1273 \pm 0.0088$
DC-CNN	$31.79 \pm 1.17$	$81.90 \pm 4.16$	$0.0389 \pm 0.0031$	$27.62 \pm 1.15$	$67.21 \pm 4.92$	$0.1023 \pm 0.0091$
CRNN	$33.95 \pm 1.38$	$87.24 \pm 5.14$	$0.0281 \pm 0.0062$	$28.85 \pm 1.34$	$72.38 \pm 5.54$	$0.0819 \pm 0.0083$
MDAMF (ours)	<b><math>35.06 \pm 1.19</math></b>	<b><math>89.40 \pm 4.13</math></b>	<b><math>0.0238 \pm 0.0048</math></b>	<b><math>30.46 \pm 1.22</math></b>	<b><math>78.40 \pm 4.57</math></b>	<b><math>0.0468 \pm 0.0075</math></b>

To address these issues, we propose a Multi-Resolution Fusion (MRF) module, as shown in Fig. 4. The MRF module is inspired by HRNet [32] and utilizes a high-resolution subnetwork as the first stage, with the number of stages gradually increasing from high resolution to low resolution. Multiple resolution subnets are parallelly connected, and multiple multi-resolution fusions are performed to enable each representation to receive information from other parallel representations repeatedly. This approach yields rich high-resolution representations, making reconstruction details more accurate and spatially precise. While Transformers [33] can capture global semantic information, their computation is intensive. In the MRF module, we utilize Swin-Transformer [34] in the low-resolution branches to capture advanced global features contained in the feature maps of the two branches. Finally, the MRF module fuses the features of three different resolutions to extract more effective high-level semantic features while maintaining resolution. Additionally,

the MRF module employs  $2 \times 2$  max pooling with a stride of 2 for downsampling and  $2 \times$  bilinear interpolation for upsampling.

### 3. Experiments and Results

#### 3.1. Dataset and training details

We validate the proposed method on two public cine MR datasets. The two datasets are ACDC [35] and SACMRI [36]. The automated cardiac diagnosis challenge (ACDC) dataset was created from real clinical exams acquired at the University Hospital of Dijon. The dataset consists of 150 exams (all from different patients), and the exams are divided into five categories, including normal case, heart failure with infarction, dilated cardiomyopathy, hypertrophic cardiomyopathy, and abnormal right ventricle. The short-axis cardiac MRI (SACMRI) dataset is provided by The Hospital for Sick

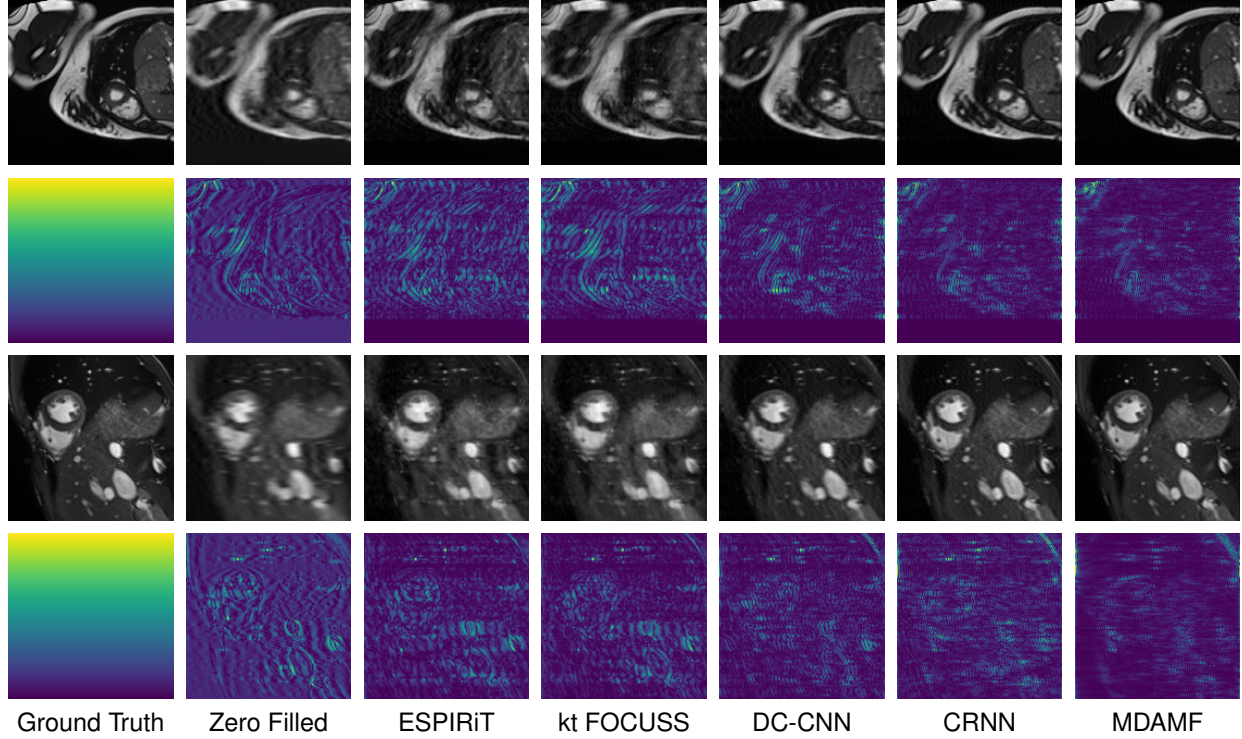


Figure 5: Qualitative comparison results of different methods on the ACDC dataset under 4 $\times$  acceleration.

Table 2: Quantitative comparison results on the SACMRI dataset.

Method	4 $\times$			8 $\times$		
	PSNR (dB) $\uparrow$	SSIM (%) $\uparrow$	NMSE $\downarrow$	PSNR (dB) $\uparrow$	SSIM (%) $\uparrow$	NMSE $\downarrow$
undersample	28.53	84.41	0.0671	25.15	76.94	0.1232
ESPIRiT	$29.10 \pm 1.79$	$85.31 \pm 4.32$	$0.0536 \pm 0.0068$	$26.45 \pm 1.55$	$77.64 \pm 4.92$	$0.0851 \pm 0.0073$
kt FOCUSS	$29.48 \pm 1.99$	$86.02 \pm 4.58$	$0.0482 \pm 0.0075$	$26.79 \pm 1.54$	$78.56 \pm 5.12$	$0.0798 \pm 0.0085$
DC-CNN	$31.63 \pm 1.81$	$89.70 \pm 4.42$	$0.0287 \pm 0.0039$	$28.11 \pm 1.26$	$83.28 \pm 4.26$	$0.0568 \pm 0.0093$
CRNN	$32.42 \pm 1.62$	$91.08 \pm 5.14$	$0.0260 \pm 0.0051$	$28.98 \pm 1.44$	$85.11 \pm 4.83$	$0.0536 \pm 0.0042$
MDAMF (ours)	<b><math>33.95 \pm 1.54</math></b>	<b><math>92.95 \pm 4.52</math></b>	<b><math>0.0235 \pm 0.0043</math></b>	<b><math>30.04 \pm 1.18</math></b>	<b><math>87.65 \pm 4.20</math></b>	<b><math>0.0473 \pm 0.0072</math></b>

Children in Toronto and consists of cardiac MR images obtained from 33 subjects.

The images in the dataset were transformed using a two-dimensional discrete Fourier transform (DFT) into the frequency domain, and spectrum centering was performed on them. Subsequently, we applied one-dimensional Gaussian downsampling templates to the fre-

quency domain data. These templates include 25% and 12.5%, simulating 4 $\times$  and 8 $\times$  acceleration in magnetic resonance sampling, respectively. After downsampling, a substantial number of streaking artifacts will appear to simulate motion artifacts during free breathing.

We designed our model based on the machine learning framework PyTorch1.12.1 using Python3.8. In particu-

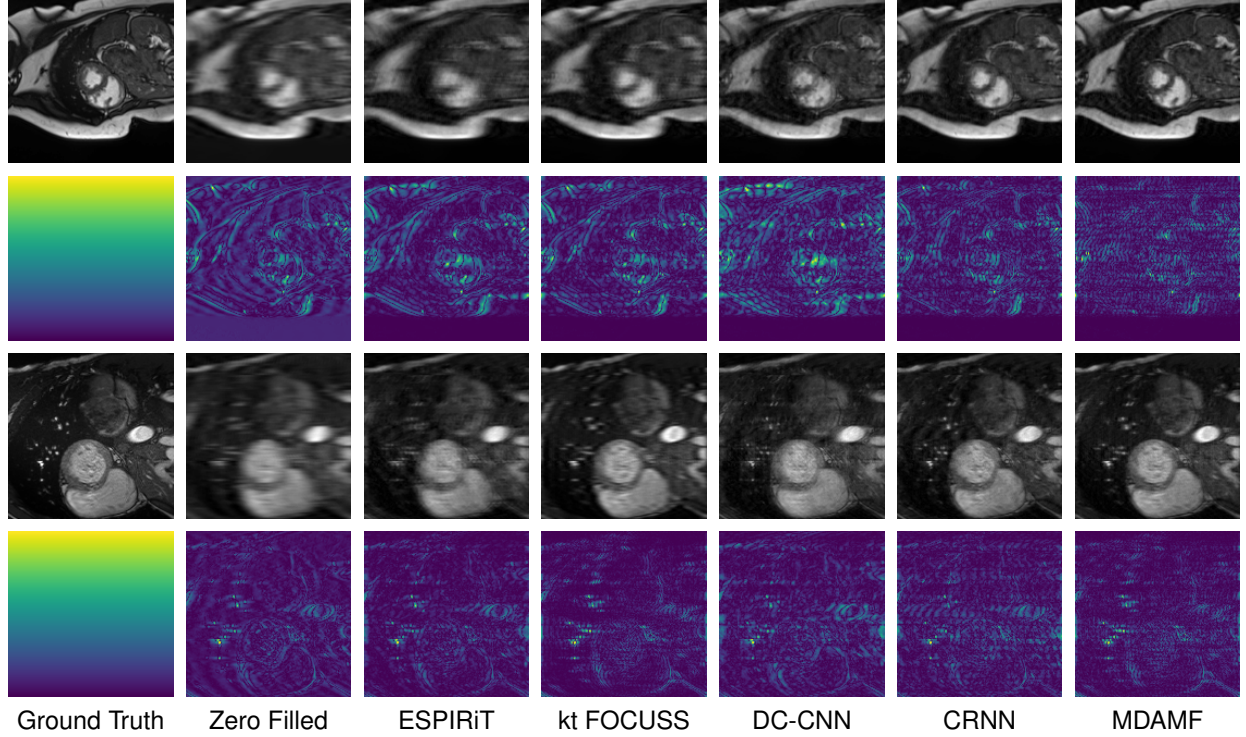


Figure 6: Qualitative comparison results of different methods on the ACDC dataset under 8x acceleration.

lar, we also use PyTorch-Lightning1.6.5, an efficient and convenient framework based on PyTorch. We trained the proposed model on a GPU server with an Intel Core i9-10900X CPU, two 10GB Nvidia RTX3080 GPUs, 32GB RAM, and 20GB VRAM. The batch size of the data is set based on the data size to ensure maximum memory utilization. The number of threads of the data reading program is 16. The initial learning rate is 1e-3. The learning rate dynamic adjustment strategy is ReduceLROnPlateau. The optimizer is AdamW [37]. The training epoch number is 100. Train with automatic mixed precision. The loss function used is the Mean Square Error (MSE) Loss (L2 Loss).

To evaluate the quality of the proposed method for cine MR image reconstruction, two commonly used image quality evaluation metrics were selected, namely the Structural Similarity Index (SSIM) [38] and Peak Signal-to-Noise Ratio (PSNR).

SSIM is based on the computations of luminance, contrast and structure terms between image  $x$  and  $y$ :

$$SSIM(x, y) = \frac{(2\mu_x\mu_y + c_1)(2\sigma_{xy} + c_2)}{(\mu_x^2 + \mu_y^2 + c_1)(\sigma_x^2 + \sigma_y^2 + c_2)} \quad (12)$$

where  $\mu_x$ ,  $\mu_y$ ,  $\sigma_x$ ,  $\sigma_y$  and  $\sigma_{xy}$  are the local means, standard deviations, and cross-covariance for images  $x$  and  $y$ , respectively.  $c_1 = (k_1 L)^2$  and  $c_2 = (k_2 L)^2$ , where  $L$  is the dynamic range of the pixel-values,  $k_1 = 0.01$  and  $k_2 = 0.03$ .

Additionally, the performance of the model was measured statistically with PSNR. It is calculated via the MSE as:

$$PSNR = 10 \lg \frac{\mathcal{R}^2}{MSE} \quad (13)$$

where  $\mathcal{R}$  is the maximum fluctuation in the input image.

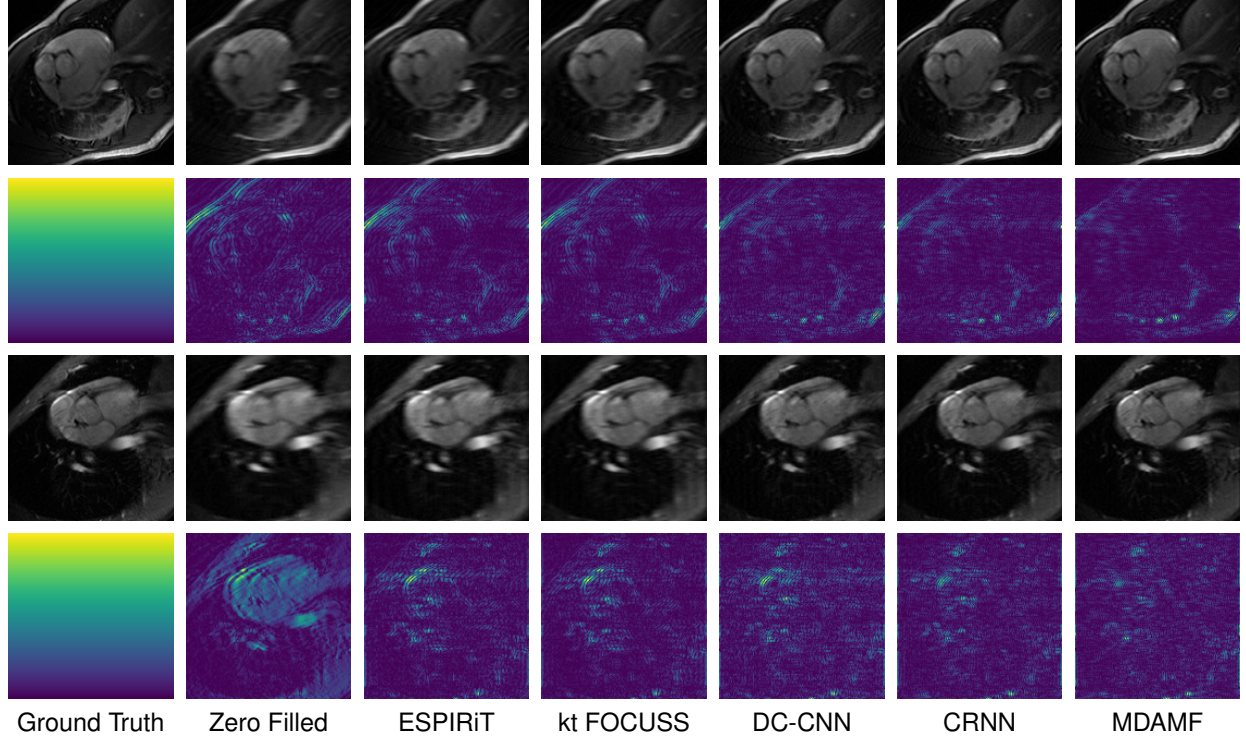


Figure 7: Qualitative comparison results of different methods on the SACMRI dataset under 4 $\times$  acceleration.

### 3.2. Results

The proposed method is compared with other mainstream Cine MRI reconstruction methods, namely ESPIRiT [39], kt FOCUSS [40], DC-CNN [16], and CRNN [17]. ESPIRiT and kt FOCUSS are based on compressed sensing, whereas DC-CNN and CRNN rely on deep learning. To ensure a fair comparison, identical settings were employed for training on both the ACDC dataset and SACMRI dataset.

The quantitative comparison between the proposed method and other methods on the ACDC dataset is presented in Table 1. The first row shows the metrics for the undersampled images reconstructed directly from zero-filled k-space. The proposed method outperforms other methods at both 4 $\times$  and 8 $\times$  acceleration rates. Specifically, at 4 $\times$  acceleration, the proposed method improves the SSIM metric by 2.16% and the PSNR metric by 1.11 dB compared to the best-performing CRNN model among

other models. The data visualization is shown in Fig. 9. At 8 $\times$  acceleration, the proposed method improves the SSIM metric by 6.02% and the PSNR metric by 1.61 dB compared to the best-performing CRNN model among other models. The data visualization is shown in Fig. 10. Clearly, the proposed method exhibits greater improvement in reconstruction performance at higher acceleration rates.

We visualized the errors between the reconstructed images and the Ground Truth using different methods on the ACDC dataset under 4 $\times$  and 8 $\times$  acceleration conditions, as shown in Figs. 5 and 6. It is evident that CS-based methods exhibit striped artifacts and significant reconstruction errors. The results obtained from DC-CNN and CRNN, which are based on deep learning, still contain substantial errors due to inadequate utilization of motion information. In contrast, our proposed method eliminates blurry artifacts and restores more fine details.

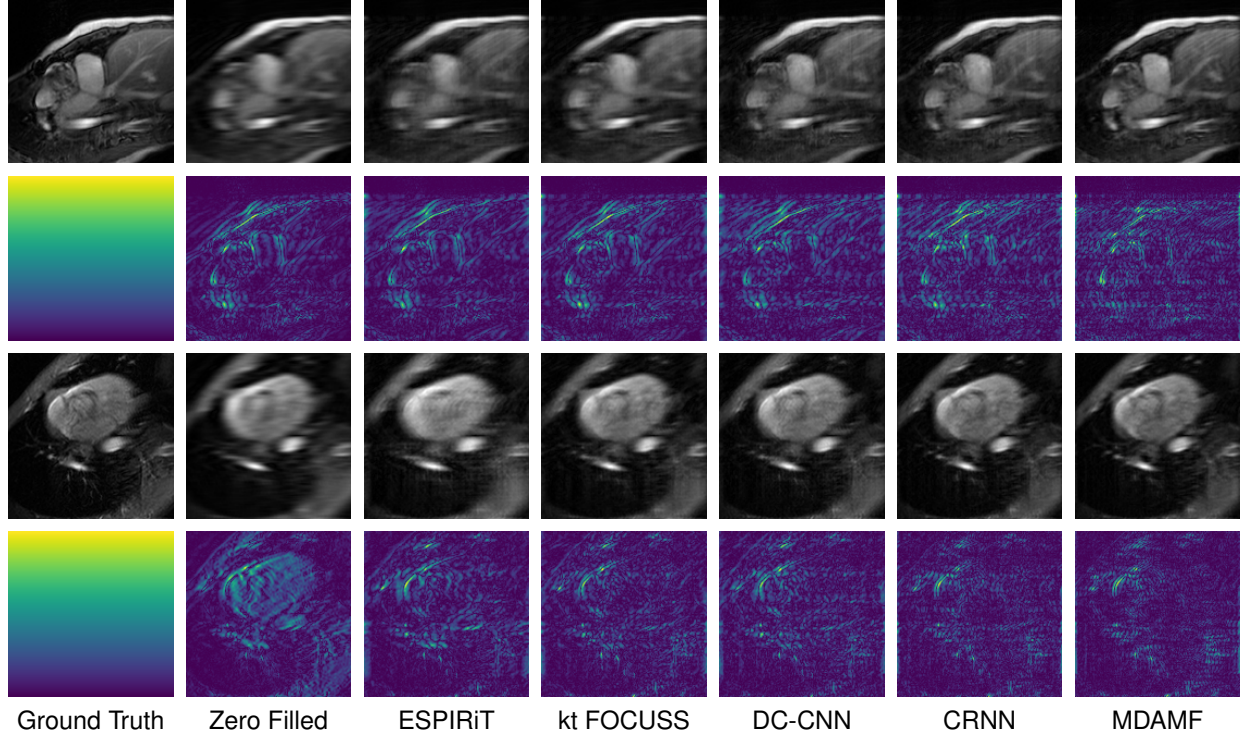


Figure 8: Qualitative comparison results of different methods on the SACMRI dataset under 8 $\times$  acceleration.

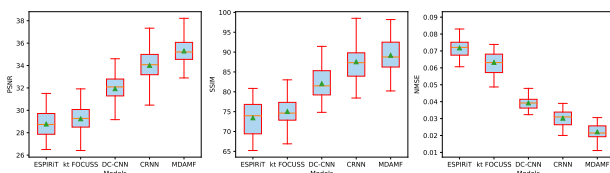


Figure 9: Data visualization of quantitative comparison results on the ACDC dataset under 4 $\times$  acceleration.

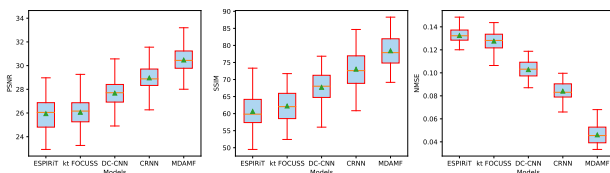


Figure 10: Data visualization of quantitative comparison results on the ACDC dataset under 8 $\times$  acceleration.

Furthermore, we also compared the aforementioned reconstruction methods on another dataset called SACMRI under 4 $\times$  and 8 $\times$  acceleration conditions, as shown in Table 2. Similar to Table 1, the first row presents the metrics for the undersampled images reconstructed directly from zero-filled k-space. Similarly, the proposed method outperforms other methods at both 4 $\times$  and 8 $\times$  acceleration rates in SACMRI. Specifically, at 4 $\times$  acceleration, the proposed method improves the SSIM metric by 1.87% and the PSNR metric by 1.53 dB compared to the best-performing CRNN model among other models. The data visualization can be seen in Fig. 11. At 8 $\times$  acceleration, the proposed method improves the SSIM metric by 2.54% and the PSNR metric by 1.06 dB compared to the best-performing CRNN model among other models. The data visualization is shown in Fig. 12. Clearly, this further demonstrates the superiority of the proposed method.

Following the same approach as in the ACDC dataset,

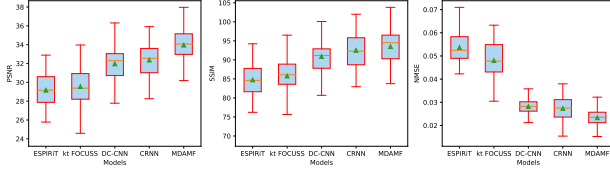


Figure 11: Data visualization of quantitative comparison results on the SACMRI dataset under 4 $\times$  acceleration.

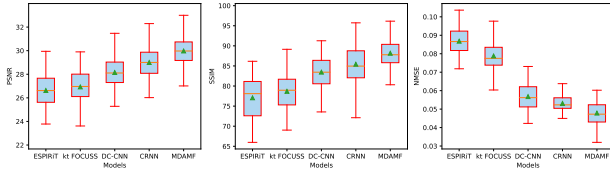


Figure 12: Data visualization of quantitative comparison results on the SACMRI dataset under 8 $\times$  acceleration.

we visualized the errors between the images reconstructed by various methods on the SACMRI dataset under 4 $\times$  and 8 $\times$  acceleration conditions and the Ground Truth, as shown in Figs. 7 and 8. Clearly, the proposed method exhibits stronger reconstruction capability for capturing details compared to other methods, and it also demonstrates a strong ability to remove artifacts.

### 3.3. Ablation study

We investigated the impact of two key modules, MGDA and MRF, on the performance of MDAMF on the ACDC dataset, as shown in Table 3. When used individually, both MGDA and MRF perform worse than MDAMF. MGDA compensates for motion artifacts in the current frame by capturing features from different reference frames, resulting in a certain performance improvement. Additionally, the powerful feature fusion or artifact correction capability of MRF contributes to a greater enhancement in the reconstruction performance of the model.

In addition, we conducted an ablation study on the second-order lattice propagation in MGDA, comparing it with first-order lattice propagation, as shown in Table 4. Experimental results demonstrate that the second-order propagation exhibits stronger competitiveness as it allows the current frame to acquire information from multiple support frames for compensation.

Table 3: The effect of MGDA and MRF on the performance of MDAMF on the ACDC dataset.

MGDA MRF	4 $\times$			8 $\times$			
	PSNR	SSIM	NMSE	PSNR	SSIM	NMSE	
✓	34.12	87.98	0.0256	28.92	74.04	0.0765	
	✓	34.45	88.27	0.0248	29.54	75.93	0.0687
✓	✓	<b>35.06</b>	<b>89.40</b>	<b>0.0238</b>	<b>30.46</b>	<b>78.40</b>	<b>0.0468</b>

Table 4: Effect of first-order propagation (FOP) and second-order propagation (SOP) on the performance of MDAMF.

FOP SOP	4 $\times$			8 $\times$			
	PSNR	SSIM	NMSE	PSNR	SSIM	NMSE	
✓	34.86	88.48	0.0247	29.10	76.54	0.0598	
	✓	<b>35.06</b>	<b>89.40</b>	<b>0.0238</b>	<b>30.46</b>	<b>78.40</b>	<b>0.0468</b>

We also conducted an ablation study on the MRF module. Since the proposed MRF module adopts a hybrid architecture of CNN and Transformer, we investigated the impact of using either the entire Transformer or the entire CNN on the model’s performance, as shown in Table 5. The experimental results indicate that using either CNN or Transformer alone does not yield satisfactory performance, while the hybrid architecture of MRF demonstrates excellent performance.

Table 5: The impact of different MRF architectures on the model performance on the ACDC dataset.

CNN Trans	4 $\times$			8 $\times$			
	PSNR	SSIM	NMSE	PSNR	SSIM	NMSE	
✓	34.57	88.90	0.0263	29.15	76.18	0.0608	
	✓	34.48	88.62	0.0258	29.29	76.45	0.0589
✓	✓	<b>35.06</b>	<b>89.40</b>	<b>0.0238</b>	<b>30.46</b>	<b>78.40</b>	<b>0.0468</b>

## 4. Discussion

The qualitative and quantitative results of the experiments indicate that the proposed method has several advantages and good generalization. The proposed method’s excellent performance can be attributed to three reasons. Firstly, the motion-guided variability alignment

has strong exploration ability, which avoids the adverse effects on the model caused by incorrect motion estimation. Secondly, the second-order bidirectional propagation avoids the attenuation of aligned features that are far or in the future caused by continuous alignment, which enables the extraction of more spatial location features when aligning the current frame and the refinement of detailed features. Thirdly, the multi-resolution fusion module can eliminate alignment errors and further eliminate artifacts.

Despite the advantages, the proposed method has some limitations. The data used in this study are all from public datasets, and the downsampled data and free-breathing data are simulated. Therefore, collecting data in real scenarios is necessary in future studies. Additionally, the proposed method has a complex network structure that requires high computational performance. Thus, reducing the computational cost and improving the method's complexity are essential for future work.

## 5. Conclusion

This paper presents a method, called MDAMF, for reconstructing cardiac cine magnetic resonance imaging under free breathing. The proposed method consists of two modules: motion-guided deformable alignment (MGDA) and multi-resolution fusion (MRF). Specifically, MGDA introduces second-order bidirectional grid propagation, while MRF is a hybrid architecture of Transformer and CNN. The experimental results demonstrate that the proposed method exhibits excellent reconstruction and anti-aliasing capabilities, as well as good generalization ability, under two different acceleration conditions (4 $\times$  and 8 $\times$ ) on two distinct datasets (ACDC and SACMRI). In future work, we will endeavor to enhance the proposed method's efficiency and performance.

## References

- [1] M. R. Patel, R. A. Klufas, Gradient-and spin-echo mr imaging of the brain, *American Journal of Neuroradiology* 20 (7) (1999) 1381–1383.
- [2] A. Deshmane, V. Gulani, M. A. Griswold, N. Seibertlich, Parallel mr imaging, *Journal of Magnetic Resonance Imaging* 36 (1) (2012) 55–72.
- [3] M. Lustig, D. Donoho, J. M. Pauly, Sparse mri: The application of compressed sensing for rapid mr imaging, *Magnetic Resonance in Medicine: An Official Journal of the International Society for Magnetic Resonance in Medicine* 58 (6) (2007) 1182–1195.
- [4] A. Balachandrasekaran, G. Ongie, M. Jacob, Accelerated dynamic mri using structured low rank matrix completion, in: 2016 IEEE International Conference on Image Processing (ICIP), IEEE, 2016, pp. 1858–1862.
- [5] S. Poddar, M. Jacob, Dynamic mri using smoothness regularization on manifolds (storm), *IEEE transactions on medical imaging* 35 (4) (2015) 1106–1115.
- [6] S. Wang, Z. Su, L. Ying, X. Peng, S. Zhu, F. Liang, D. Feng, D. Liang, Accelerating magnetic resonance imaging via deep learning, in: 2016 IEEE 13th international symposium on biomedical imaging (ISBI), IEEE, 2016, pp. 514–517.
- [7] D. Lee, J. Yoo, S. Tak, J. C. Ye, Deep residual learning for accelerated mri using magnitude and phase networks, *IEEE Transactions on Biomedical Engineering* 65 (9) (2018) 1985–1995.
- [8] B. Zhu, J. Z. Liu, S. F. Cauley, B. R. Rosen, M. S. Rosen, Image reconstruction by domain-transform manifold learning, *Nature* 555 (7697) (2018) 487–492.
- [9] L. Xiang, Y. Chen, W. Chang, Y. Zhan, W. Lin, Q. Wang, D. Shen, Deep-learning-based multimodal fusion for fast mr reconstruction, *IEEE Transactions on Biomedical Engineering* 66 (7) (2018) 2105–2114.
- [10] Y. Han, L. Sunwoo, J. C. Ye, k-space deep learning for accelerated mri, *IEEE transactions on medical imaging* 39 (2) (2019) 377–386.
- [11] M. Ran, J. Hu, Y. Chen, H. Chen, H. Sun, J. Zhou, Y. Zhang, Denoising of 3d magnetic resonance images using a residual encoder–decoder wasserstein generative adversarial network, *Medical image analysis* 55 (2019) 165–180.

[12] F. Odille, P.-A. Vuissoz, P.-Y. Marie, J. Felblinger, Generalized reconstruction by inversion of coupled systems (grics) applied to free-breathing mri, *Magnetic Resonance in Medicine: An Official Journal of the International Society for Magnetic Resonance in Medicine* 60 (1) (2008) 146–157.

[13] H. Chandarana, L. Feng, J. Ream, A. Wang, J. S. Babb, K. T. Block, D. K. Sodickson, R. Otazo, Respiratory motion-resolved compressed sensing reconstruction of free-breathing radial acquisition for dynamic liver mri, *Investigative radiology* 50 (11) (2015) 749.

[14] T. Zhang, J. Y. Cheng, A. G. Potnick, R. A. Barth, M. T. Alley, M. Uecker, M. Lustig, J. M. Pauly, S. S. Vasanawala, Fast pediatric 3d free-breathing abdominal dynamic contrast enhanced mri with high spatiotemporal resolution, *Journal of Magnetic Resonance Imaging* 41 (2) (2015) 460–473.

[15] M. Usman, B. Ruijsink, M. Nazir, G. Cruz, C. Prieto, Free breathing whole-heart 3d cine mri with self-gated cartesian trajectory, *Magnetic resonance imaging* 38 (2017) 129–137.

[16] J. Chlempner, J. Caballero, J. Hajnal, A. Price, D. Rueckert, A deep cascade of convolutional neural networks for dynamic mr image reconstruction, *IEEE Transactions on Medical Imaging* 37 (2017) 491–503.

[17] C. Qin, J. Schlemper, J. Caballero, A. N. Price, J. V. Hajnal, D. Rueckert, Convolutional recurrent neural networks for dynamic mr image reconstruction, *IEEE transactions on medical imaging* 38 (1) (2018) 280–290.

[18] C. Sarasaen, S. Chatterjee, M. Breitkopf, G. Rose, A. Nürnberger, O. Speck, Fine-tuning deep learning model parameters for improved super-resolution of dynamic mri with prior-knowledge, *Artificial Intelligence in Medicine* 121 (2021) 102196.

[19] R. Wei, J. Chen, B. Liang, X. Chen, K. Men, J. Dai, Real-time 3d mri reconstruction from cine-mri using unsupervised network in mri-guided radiotherapy for liver cancer, *Medical Physics* (2022).

[20] E. K. Cole, F. Ong, S. S. Vasanawala, J. M. Pauly, Fast unsupervised mri reconstruction without fully-sampled ground truth data using generative adversarial networks, in: *Proceedings of the IEEE/CVF International Conference on Computer Vision*, 2021, pp. 3988–3997.

[21] J. Yoo, K. H. Jin, H. Gupta, J. Yerly, M. Stuber, M. Unser, Time-dependent deep image prior for dynamic mri, *IEEE Transactions on Medical Imaging* 40 (12) (2021) 3337–3348.

[22] G. Seegoolam, J. Schlemper, C. Qin, A. Price, J. Hajnal, D. Rueckert, Exploiting motion for deep learning reconstruction of extremely-undersampled dynamic mri, in: *Medical Image Computing and Computer Assisted Intervention–MICCAI 2019: 22nd International Conference, Shenzhen, China, October 13–17, 2019, Proceedings, Part IV*, Springer, 2019, pp. 704–712.

[23] Q. Huang, Y. Xian, D. Yang, H. Qu, J. Yi, P. Wu, D. N. Metaxas, Dynamic mri reconstruction with end-to-end motion-guided network, *Medical Image Analysis* 68 (2021) 101901.

[24] C. Eldeniz, W. Gan, S. Chen, T. J. Fraum, D. R. Ludwig, Y. Yan, J. Liu, T. Vahle, U. Krishnamurthy, U. S. Kamilov, et al., Phase2phase: respiratory motion-resolved reconstruction of free-breathing magnetic resonance imaging using deep learning without a ground truth for improved liver imaging, *Investigative Radiology* 56 (12) (2021) 809–819.

[25] J. F. Kunz, S. Ruschke, R. Heckel, Implicit neural networks with fourier-feature inputs for free-breathing cardiac mri reconstruction, *arXiv preprint arXiv:2305.06822* (2023).

[26] E. J. Zucker, C. M. Sandino, A. Kino, P. Lai, S. S. Vasanawala, Free-breathing accelerated cardiac mri using deep learning: validation in children and young adults, *Radiology* 300 (3) (2021) 539–548.

[27] S. Biswas, H. K. Aggarwal, S. Poddar, M. Jacob, Model-based free-breathing cardiac mri reconstruction using deep learned & storm priors: Modl-storm,

in: 2018 IEEE International Conference on Acoustics, Speech and Signal Processing (ICASSP), IEEE, 2018, pp. 6533–6537.

[28] Y. Tian, Y. Zhang, Y. Fu, C. Xu, Tdan: Temporally-deformable alignment network for video super-resolution, in: Proceedings of the IEEE/CVF conference on computer vision and pattern recognition, 2020, pp. 3360–3369.

[29] J. Dai, H. Qi, Y. Xiong, Y. Li, G. Zhang, H. Hu, Y. Wei, Deformable convolutional networks, in: Proceedings of the IEEE international conference on computer vision, 2017, pp. 764–773.

[30] K. C. Chan, X. Wang, K. Yu, C. Dong, C. C. Loy, Understanding deformable alignment in video super-resolution, in: Proceedings of the AAAI conference on artificial intelligence, Vol. 35, 2021, pp. 973–981.

[31] K. C. Chan, S. Zhou, X. Xu, C. C. Loy, Bascvsr++: Improving video super-resolution with enhanced propagation and alignment, in: Proceedings of the IEEE/CVF conference on computer vision and pattern recognition, 2022, pp. 5972–5981.

[32] K. Sun, B. Xiao, D. Liu, J. Wang, Deep high-resolution representation learning for human pose estimation, in: Proceedings of the IEEE/CVF conference on computer vision and pattern recognition, 2019, pp. 5693–5703.

[33] Z. Liu, Y. Lin, Y. Cao, H. Hu, Y. Wei, Z. Zhang, S. Lin, B. Guo, Swin transformer: Hierarchical vision transformer using shifted windows, in: Proceedings of the IEEE/CVF international conference on computer vision, 2021, pp. 10012–10022.

[34] A. Vaswani, N. Shazeer, N. Parmar, J. Uszkoreit, L. Jones, A. N. Gomez, Ł. Kaiser, I. Polosukhin, Attention is all you need, *Advances in neural information processing systems* 30 (2017).

[35] O. Bernard, A. Lalande, C. Zotti, F. Cervenansky, X. Yang, P.-A. Heng, I. Cetin, K. Lekadir, O. Camara, M. A. G. Ballester, et al., Deep learning techniques for automatic mri cardiac multi-structures segmentation and diagnosis: is the problem solved?, *IEEE transactions on medical imaging* 37 (11) (2018) 2514–2525.

[36] A. Andreopoulos, J. K. Tsotsos, Efficient and generalizable statistical models of shape and appearance for analysis of cardiac mri, *Medical image analysis* 12 (3) (2008) 335–357.

[37] I. Loshchilov, F. Hutter, Fixing weight decay regularization in adam (2017).

[38] Z. Wang, A. C. Bovik, H. R. Sheikh, E. P. Simoncelli, Image quality assessment: from error visibility to structural similarity, *IEEE transactions on image processing* 13 (4) (2004) 600–612.

[39] M. Uecker, P. Lai, M. J. Murphy, P. Virtue, M. Elad, J. M. Pauly, S. S. Vasanawala, M. Lustig, Esprit—an eigenvalue approach to autocalibrating parallel mri: where sense meets grappa, *Magnetic resonance in medicine* 71 (3) (2014) 990–1001.

[40] H. Jung, K. Sung, K. S. Nayak, E. Y. Kim, J. C. Ye, k-t focuss: a general compressed sensing framework for high resolution dynamic mri, *Magnetic Resonance in Medicine: An Official Journal of the International Society for Magnetic Resonance in Medicine* 61 (1) (2009) 103–116.